



A NIR-II-emitting gold nanocluster-based drug delivery system for smartphone-triggered photodynamic theranostics with rapid body clearance

Yifei Kong^a, David Santos-Carballal^b, David Martin^b, Natalia N. Sergeeva^b, Weili Wang^{b,*}, Guishi Liu^a, Benjamin Johnson^c, Brijesh Bhayana^a, Zuantao Lin^a, Yensheng Wang^a, Xavier Le Guével^{d,*}, Nora H. de Leeuw^{b,e,f}, Dejian Zhou^{b,*}, Mei X. Wu^{a,*}

^a Wellman Center for Photomedicine, Massachusetts General Hospital, Harvard Medical School, Boston, MA 02114, United States

^b School of Chemistry, University of Leeds, Leeds LS2 9JT, United Kingdom

^c School of Physics and Astronomy, University of Leeds, Leeds LS2 9JT, United Kingdom

^d Institute for Advanced Biosciences, Université Grenoble-Alpes, INSERM U1209, CNRS UMR 5309, Allée des Alpes, 38700 La Tronche, France

^e School of Chemistry, Cardiff University, Cardiff CF10 3AT, United Kingdom

^f Department of Earth Sciences, Utrecht University, Budapestlaan 4, 3584 CD Utrecht, The Netherlands

Nanomedicine has grown structurally complex in order to perform multiple tasks at a time. However, their unsatisfied reliability, uniformity and reproducibility account for the high rates of attrition in translational research. So far, most studies have been one-sidedly focused on the treatment efficacy of inorganic nanoparticles as cancer therapeutics, but overlook their elimination from the body – a key factor in getting regulatory approval. Instead of developing a new drug nanocarrier with uncertain future in medical practice, we therefore choose to leverage the utility of promising and translatable gold nanoclusters (AuNCs) for designing a simple but robust “all-in-one” nanocluster drug delivery system, where the AuNCs not only strengthen the renal clearance of neutral red (NR) as a model drug, but also aid its passive tumor targeting *via* the enhanced permeability and retention (EPR) effect. More interestingly, NR can stimulate the production of reactive oxygen species (ROS) to suppress tumor growth under ultralow-level radiation with a smartphone’s torch (fluence rate: 8 mW/cm²). This finding is especially valuable to low- and middle-income countries lacking resources in healthcare settings. By means of first-principles simulations, we also study in-depth the energies, structural and electronic properties of the AuNCs emitting in the second near-infrared window (NIR-II, 1000–1700 nm). In brief, our model fulfills safety, effectiveness and cost-effectiveness requirements for translational development.

Keywords: NIR-II imaging; DFT calculation; Gold nanoclusters; Renal clearance; Smartphone; Photodynamic therapy

Introduction

Since the popularization of “all-in-one” strategy, nanoparticle (NP) based medicine has become increasingly complex as a result of harboring various functional modules to serve multiple purposes [1–7]. For example, a nanoplatform for image-guided

* Corresponding authors.

E-mail addresses: Wang, W. (ml07ww@leeds.ac.uk), Le Guével, X. (xavier.le-guevel@univ-grenoble-alpes.fr), Zhou, D. (d.zhou@leeds.ac.uk), Wu, M.X. (mwu5@mg.harvard.edu).

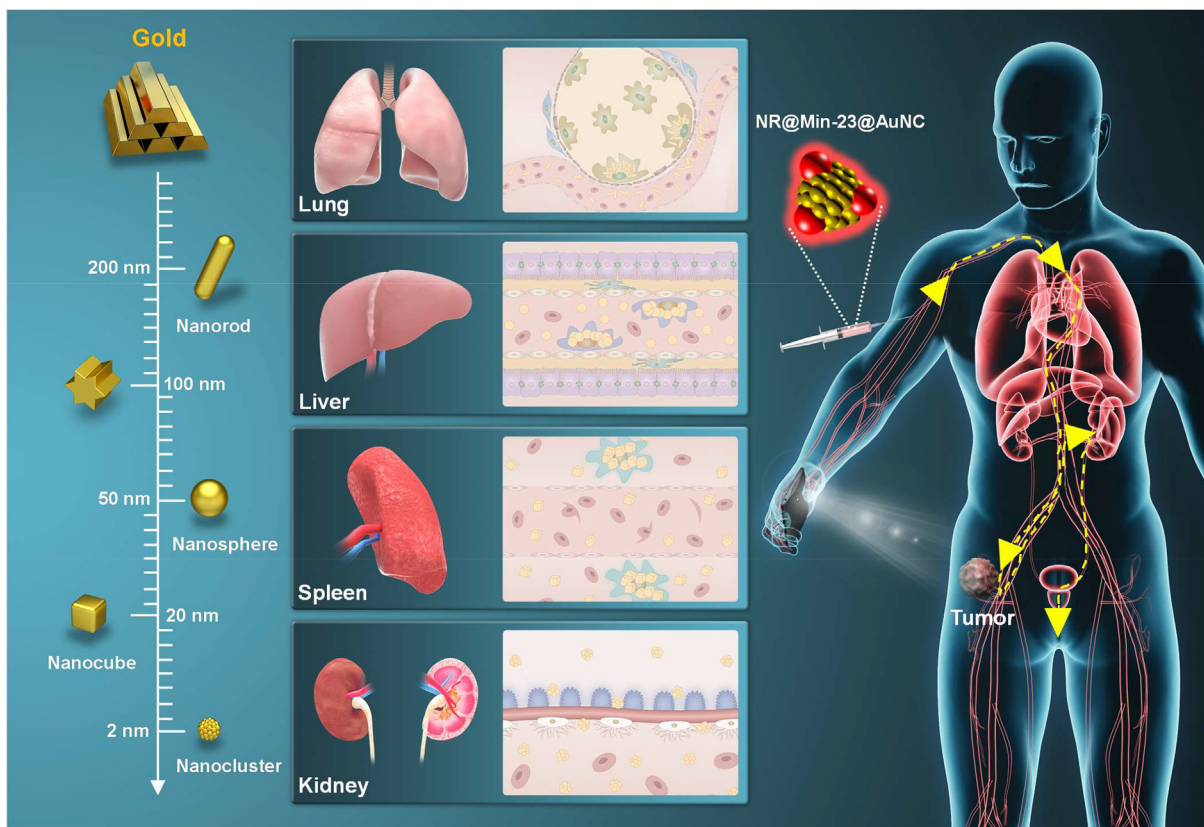
photodynamic therapy (PDT) typically consists of contrast agent, photosensitizer (PS) and targeting moiety [8]. Chemistry for incorporating such components is often cumbersome, due to which the nanoplatform tends to have poor reliability and reproducibility with a larger size than the threshold of being body-clearable. The United States Food and Drug Administration mandates medical imaging drugs only if they can be eliminated from the body within a reasonable time frame [9]. Yet this requirement has not been treated seriously.

With greater potential than many nanomaterials in clinical translation, nanogolds (*e.g.*, nanorod, nanostar, nanosphere, nanocube, *etc.*) are extensively studied in cancer theranostics [10–14]. For example, human tumor necrosis factor (TNF)-bound gold NPs (*aka* CYT-6091) were tested on cancer patients in phase I clinical trial [15]. Nanogolds in the size range of 5–200 nm, however, would be captured by the reticuloendothelial system (RES) for inefficient hepatic excretion (Scheme 1), which may compromise their utility by placing organs at the risk of chronic damage [16]. In contrast, atomic gold nanoclusters (AuNCs) with size below the kidney filtration threshold (KFT, *ca.* 5.5 nm) can be cleared rapidly *via* the kidney [17–21]. Moreover, they support easy modification and high drug loading. In a pioneering work, folate (FA) and chlorin e6 (Ce6) were bound to glutathione-coated AuNCs (GS-AuNCs) for laser-mediated PDT

on xenograft-bearing mice [22]. Despite the success, the research exposes some of its limitations: (1) emission spectral overlap between Ce6 and GS-AuNCs; (2) preferential accumulation of GS-AuNCs in RES; (3) an appreciable amount of GS-AuNCs entering brains after conjugation with FA, presumably due to FA receptors expressed at the brain-blood barrier (BBB) [23].

Regarding rational design of a gold nanocluster-based drug delivery system, we believe that simplicity should be one of principal design philosophies of all time. Zheng *et al.* completed passive tumor targeting with GS-AuNCs through the enhanced permeability and retention (EPR) effect [24,25]. Kawasaki *et al.* reported the production of reactive oxygen species (ROS) elicited by AuNCs under 532-nm laser irradiation for phototherapeutic activities [26]. These findings indicate the likelihood of merging several functions (*e.g.*, bioimaging, PDT, tumor targeting, *etc.*) into a single AuNC entity. Chen *et al.* circumvented tumor hypoxia by modifying human serum albumin (HSA)-stabilized AuNCs with catalase that decomposes endogenous H₂O₂ [27]. However, the extra protein layer may slow *in vivo* AuNC clearance [28]. To this end, we propose to label a small-molecule PS to AuNCs so that PDT efficacy can be improved without meaningful growth in size.

Fluorescence imaging in the second near-infrared window (NIR-II, $\lambda = 1000\text{--}1700\text{ nm}$) has been evolving into a hot topic



SCHEME 1

Schematic illustration of body clearance of various Au nanostructures, including nanorods, nanostars, nanospheres, nanocubes and nanoclusters, through different organs according to their sizes: aerosolic Au nanorods (>200 nm) can be filtered by lungs; Au nanospheres and nanocubes with sizes of 20–100 nm are mainly eliminated by the RES including liver and spleen; ultrasmall Au nanoclusters (<2 nm) can pass through kidney filtration for urinary excretion. In this work, NIR-II-emitting NR@Min-23@AuNCs passively accumulate in tumor as a result of the EPR effect for smartphone-triggered photodynamic therapy and hold promise of minimizing *in vivo* toxicity by rapid renal clearance.

with the first human clinical study in 2020 [29]. It holds great promise for imaging with high spatial resolution and signal-to-background ratio (SBR) in deep tissues compared with the first near-infrared window (NIR-I, $\lambda = 700\text{--}900\text{ nm}$) [30–35]. As such, it has been the subject of considerable effort devoted to the development of NIR-II nanoprobes [36–43]. Until recently, bioimaging with AuNCs have been transitioned to the NIR-II window, but most of these AuNCs demonstrate a non-ideal split emission [44–47]. Herein, we report the first use of miniprotein Min-23 in templating the synthesis of NIR-II-emitting AuNCs (abbreviated as Min-23@AuNCs). The miniprotein is a 23-mer polypeptide (LXRCKQSDCLAGSVCGPNGFCG, X = Nle) stabilized by two disulfide bridges (*i.e.* 4–16, 10–22) to afford it strong affinity for gold but without tryptophan and tyrosine residues. It folds into a cystine-stabilized β -sheet motif to give a compact 3D structure [48]. With primary amine groups in the lysine residue and N-terminus, Min-23 can provide sufficient cross-linking sites for functionalization. Since Min-23 has both positive- (R, K) and negative- (D, D) charged residues with a net neutral charge, it can serve as a zwitterionic ligand to effectively reduce non-specific absorption of serum proteins and to enhance biocompatibility [49–52]. Considering these advantageous characteristics, we have therefore chosen Min-23 for the synthesis of NIR-II-emitting AuNCs. Neutral red (NR) as an ideal small-molecule PS is engineered to carry an azido group for conjugation with Min-23@AuNCs *via* “click” reaction [53]. NR-labeled Min-23@AuNCs not only allow for EPR-mediated passive targeting and efficient renal clearance, but also can boost the ROS generation for tumor suppression upon exposure to low-dose radiation with a smartphone’s LED torch - that is, one of the most easily accessible light sources for PDT [54,55].

Results and discussion

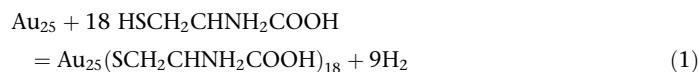
Photophysical characterizations

The absorption of Min-23@AuNCs increases monotonically towards the short wavelength without a surface plasmon resonance band at 520 nm (Fig. 1a). The gaussian-shaped emission band (λ center: 1050 nm) gets rid of peak splitting normally seen for other NIR-II-emitting AuNPs, with over half of the spectral band spreading into the NIR-II region with a full width at half maximum (FWHM) of $\sim 200\text{ nm}$. When the molar ratio of Au/Min-23 drops from 1/1.1 to 1/4.4, a blue shift of emission peak is noted (Fig. S1). This phenomenon is strongly correlated to the effect of ligands on the AuNC surface with a high contribution of the complex Au(I)-S to the emission around 930 and 1050 nm [44]. The pale-brown Min-23@AuNC suspension fluoresces intensely with a quantum yield (Φ_f) of 0.21% using IR-26 dye as reference (Fig. S2). The photoluminescence (PL) remains stable in common buffers (*i.e.* DMEM, FBS, and PBS) after a 30-day storage (Fig. S3) and insensitive to changes in pH, ionic strength and oxidant stress (Figs. S4–S6). Since Min-23 (measured Mw: 2343.7, Fig. S7) is free of tryptophan and tyrosine residues, the intrinsic fluorescence of proteins is diminished. The NIR-II PL of Min-23@AuNCs with relatively long lifetimes - $\tau_1 = 183 \pm 2.2\text{ ns}$ ($\sim 61\%$), $\tau_2 = 903 \pm 9.4\text{ ns}$ ($\sim 39\%$), and $R^2 = 0.997$ - emanates from ligand-to-metal charge transfer (LMCT) and/or ligand-to-metal-metal charge transfer (LMMCT) transitions *via* the Au(I)-

S coordination (Fig. 1b). X-ray photoelectron spectroscopy (XPS) is deconvoluted into two distinct components of Au(0) and Au(I) to show the presence of the Au(I)-S shell with $<20\%$ of Au(I) on the Au(0) core, where the signatures of Au 4f doublet locate at 83.7 eV for 4f_{7/2} and 87.4 eV for 4f_{5/2} (Fig. 1c). Moreover, the core diameter (d) of AuNCs, which, at $1.81 \pm 0.26\text{ nm}$ (Fig. 1d), is significantly smaller than that of most inorganic NIR-II nanoprobes [42,56,57].

Density functional theory (DFT) calculation

We note that AuNCs prepared by LA-sulfobetaine by Chen et al. [47] or Min-23 by us have similar gaussian-shaped emission spectra peaking at $\sim 1000\text{ nm}$ with the Φ_f s in the same range (Table S1). The number of Au atoms measured for Chen et al.’s AuNCs is 20–50, while that for ours is 16–27 (Fig. S8). As reported by Liu et al., the Au₂₅ clusters consisting of 25 atoms fluoresce in the NIR-II region [13]. We thus speculated that the number of gold atom of Min-23@AuNCs that contribute to the NIR-II emission is also twenty-five. However, we did not see the specific absorption band of the Au₂₅ cluster at 680 nm in the absorbance spectra of LA-sulfobetaine capping AuNCs and Min-23@AuNCs. The plausible reason may arise in the low content of the Au₂₅ species in both models, interpreting their relatively low Φ_f s. Each Min-23 ligand contains four L-cysteine residues (4 HSCH₂-CHNH₂COOH groups) and a Min-23: Au molar ratio of $\sim 1.05:1$ was used for the synthesis, therefore there were sufficient SCH₂-CHNH₂COOH groups to form the most stable Au₂₅(SCH₂-CHNH₂COOH)₁₈ cluster. Taking the Au₂₅(SR)₁₈ cluster (SR = SCH₂CHNH₂COOH) as the model system, we studied the energies, structural and electronic properties by means of first-principles simulations. We inspected the formation of the cluster, corresponding to the following chemical reaction:



where the isolated reactant and product species, *i.e.* the icosahedron core containing the 12 capping Au atoms (Au₂₅), the L-cysteine residue (HSCH₂CHNH₂COOH), the thiolated cluster [Au₂₅(SCH₂CHNH₂COOH)₁₈] and the hydrogen molecule (H₂), were modelled in cells which were large enough to avoid spurious interactions with their periodically repeated images. We also assumed that in Eq. (1) both the isolated Au₂₅ cluster and the thiolated Au₂₅(SCH₂CHNH₂COOH)₁₈ cluster have the same geometry.

The calculated exothermic formation energy per L-cysteine residue is -2.206 eV , indicating that Eq. (1) is feasible under thermodynamic grounds. Our calculated formation energy per L-cysteine residue is at least 1 eV more favourable than the interaction of this adsorbate with the two highly reactive chiral Au (321)^{RS} surfaces [58]. Moreover, the formation of a highly stable self-assembled monolayer (SAM) of nitronyl nitroxide radical thiols with the doublet and quartet magnetic states, which are almost degenerate in energy, releases approximately 1.8 eV on the Au(111) surface reconstructed with one Au adatom [59]. Even the largest binding energy reported for a deprotonated L-cysteine molecule on a Au₄ aggregate is only -1.7 eV [60]. Therefore, our calculated negative formation energy provides evidence that using the capping thiol groups of L-cysteine is an effective route

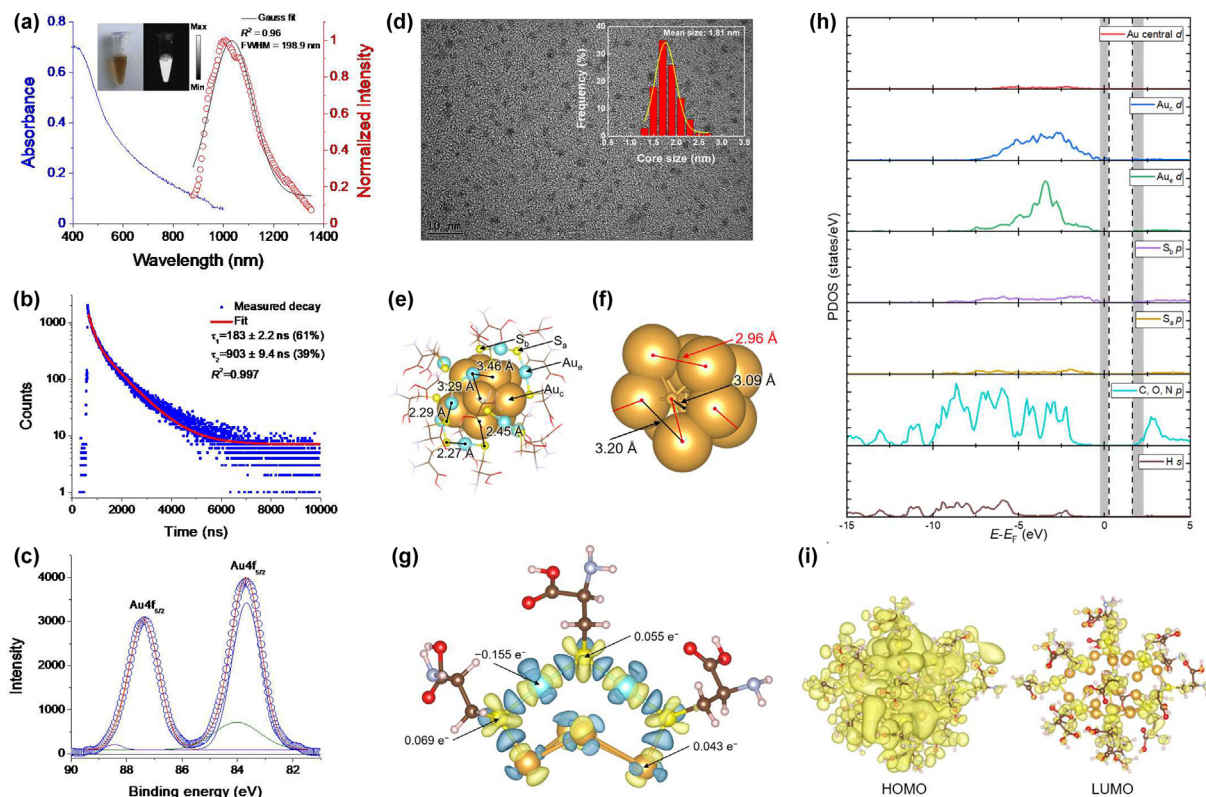


FIGURE 1

Photophysical characterization and density functional theory (DFT) calculation. (a) Absorption (blue line) and normalized fluorescence (red line) spectra of Min-23@AuNCs ($\lambda_{\text{ex}} = 808$ nm). Inset shows bright-field (left) and dark-field (right) images of the Min-23@AuNC suspension under natural light and 808-nm laser. (b) Fluorescence decay curve of Min 23@AuNCs dispersed in water [bi-exponential fit, $\tau_1 = 183 \pm 2.2$ ns (61%), $\tau_2 = 903 \pm 9.4$ ns (39%), $R^2 = 0.997$]. (c) XPS spectrum in the Au 4f region. (d) TEM image of AuNCs. Inset shows histogram of particle size distribution (core size, $d = 1.81 \pm 0.26$ nm; polydispersity index, PDI = 0.02). Optimized structure of (e) the $\text{Au}_{25}(\text{SCH}_2\text{CHNH}_2\text{COOH})_{18}$ cluster and (f) icosahedral Au_{13} core. Core Au (Au_c) is in dark yellow, external Au (Au_e) is in cyan, base S (S_b) and apex S (S_a) are in light yellow, O is in red, N is in blue, C is in grey and H is in white. Au_{13} core is in space-filling balls, $-(\text{S}-\text{Au}-\text{S}-\text{Au}-\text{S})-$ staple group is in ball-and-stick and the $\text{CH}_2\text{CHNH}_2\text{COOH}$ fragment is in wireframe. One of the external atoms and the central Au atom in (f) are displayed as ball-and-stick to allow a view of the cluster cavity. The red lines connecting the Au_c atoms in (f) indicate the 6 short bonds below the staple capping groups. (g) Charge density flow ($\Delta\rho$) for the binding of 18 $\text{SCH}_2\text{CHNH}_2\text{COOH}$ residues on the $\text{Au}_{25}(\text{SCH}_2\text{CHNH}_2\text{COOH})_{17}$ cluster. For clarity, only two neighboring triangular faces of the Au_{25} icosahedron cluster and the capping $-(\text{SR}-\text{Au}-\text{SR}-\text{Au}-\text{SR})-$ staple group, where $\text{R} = \text{CH}_2\text{CHNH}_2\text{COOH}$ are shown. Electron density gain and depletion surfaces are in blue and yellow, respectively. Isosurfaces display a value of $\pm 0.005 \text{ e} \text{ \AA}^{-3}$. The atomic charge density difference for the atoms that suffered the largest change are also indicated. A negative value of charge transfer denotes that the species gains electron charge. All atoms are represented in ball-and-stick. Core Au_c is in dark yellow, external Au_e is in cyan, base S_b and apex S_a are in light yellow, O is in red, N is in blue, C is in grey and H is in white. (h) Atomic projections of the electronic density of states (PDOS) and (i) representation of the highest occupied molecular orbital (HOMO) and lowest unoccupied molecular orbital (LUMO) for the $\text{Au}_{25}(\text{SCH}_2\text{CHNH}_2\text{COOH})_{18}$ cluster. Isosurfaces display a value of $0.0015 \text{ e} \text{ \AA}^{-3}$. All atoms are represented in ball-and-stick. Core Au_c is in dark yellow, external Au_e is in cyan, base S_b and apex S_a are in light yellow, O is in red, N is in blue, C is in grey and H is in white. The dashed vertical lines indicate the position of the valence band maximum (VBM) and conduction band minimum (CBM).

to stabilize the unique structure of the Au_{25} cluster, which is a testament of its easy functionalisation, in line with our experiments.

We next investigated the ground state equilibrium geometry of the thiolated $\text{Au}_{25}(\text{SCH}_2\text{CHNH}_2\text{COOH})_{18}$ cluster. Our starting point is the crystal structure of the $\text{Au}_{25}(\text{SCH}_2\text{CH}_2\text{Ph})_{18}$ cluster determined by Heaven et al. containing an icosahedral Au_{13} core capped by 6 $-(\text{SR}-\text{Au}-\text{SR}-\text{Au}-\text{SR})-$ staple groups [61], where we replaced the R groups by the $\text{CH}_2\text{CHNH}_2\text{COOH}$ fragment (Fig. 1e). The $\text{Au}_{25}\text{S}_{18}$ central section of the nanoparticle has approximately the point group D_{2h} , characterized by three mutually orthogonal C_2 axes, which lie along the line connecting the centre of the nanoparticle with the opposite apex S atoms (S_a), plus three horizontal mirror planes (σ_h) perpendicular to C_2 . Fig. 1f displays the average interatomic distance (d) calculated

at 3.09 \AA between the central atom and the remaining twelve core Au atoms (Au_c). There are two types of connections between the core Au_c atoms, *i.e.*, 6 short bonds of approximately 2.96 \AA below the staple capping groups and 24 longer bonds with a mean distance of 3.20 \AA . The external Au_e atoms capping 3/5 of the twenty triangular faces of the icosahedron are located 3.29 and 3.46 \AA away from the two closest and the more distant Au_c atom, respectively. We also found that $d_{\text{S}_a-\text{Au}_e} = 2.27 \text{ \AA}$, which is very close to the 2.29 \AA between the base S (S_b) and Au_e atoms. However, the S_b-Au_c distance is $\sim 0.17 \text{ \AA}$ larger than for both S_a-Au_e and S_b-Au_e bonds, indicating that the covalent forces between the atoms within the staple groups are stronger than between the Au_{13} core and the capping fragment. Our interatomic distances simulated are overestimated by only 0.15 , 0.24 , and 0.30 \AA for the short Au_c-Au_c bond, long Au_c-Au_c bond and

the bond between the central atom and neighbouring Au atoms, respectively, with respect to the values based on the X-ray crystal structure of the ionic and well packed $[\text{N}(\text{C}_8\text{H}_{17})_4][\text{Au}_{25}(\text{SCH}_2\text{-CH}_2\text{Ph})_{18}]$ [61]. The simulated $\text{Au}_c\text{-S}_b$ bond is just 0.07 Å larger than the value previously reported, whereas our $\text{Au}_e\text{-S}_a$ and $\text{Au}_e\text{-S}_b$ distances are slightly underestimated by 0.04 Å [61]. Both, the short and long $\text{Au}_c - \text{Au}_e$ distances are also overestimated by up to 0.2 Å with respect to experimental studies on a $\text{Au}_{25}(\text{SR})_{18}$ analogue [62]. Despite the small structural differences between our calculations for an isolated cluster and experiments, our simulations are able to predict the correct interatomic bond distance trends.

We examined the impact on the electronic properties of the binding of the L-cysteine residue on the Au_{25} cluster. The Bader analysis indicates that each $-\text{SCH}_2\text{CHNH}_2\text{COOH}$ fragment donates an average of 0.070 e^- to the Au_{25} cluster, which becomes negatively charged by $-1.264 e^-$. To provide further insight into the electron transfer mechanism that takes place during the adsorption process, we have also plotted the charge density flow ($\Delta\rho$). $\Delta\rho$ has been defined as the total charge density of $\text{Au}_{25}(\text{SCH}_2\text{CHNH}_2\text{COOH})_{18}$ minus the sum of the charge density of the isolated interacting species, *i.e.* 18 $\text{SCH}_2\text{CHNH}_2\text{COOH}$ groups and the Au_{25} cluster, all in the same geometry. Fig. 1g illustrates $\Delta\rho$ for a section of the cluster comprising one $-(\text{SR}-\text{Au}-\text{SR}-\text{Au}-\text{SR})-$ staple group, where $R = \text{CH}_2\text{CHNH}_2\text{COOH}$, and two nearby triangular faces of the Au_{25} icosahedron cluster. The electron charge density pathway indicates that the external Au_e atoms, that gained an average of $-0.155 e^-$, are the net receivers during the adsorption of the L-cysteine residues. The simulations suggest that the apex S_a and base S_b atoms donate slightly different amounts of charge, that differ by 0.014 e^- . Interestingly, the core Au_c atoms also transfer 0.043 e^- of charge, *via* S_b , to the Au_e atoms. Both the Bader analysis and charge density difference show that the electronic properties of the R fragment experience a negligible change during the adsorption of the L-cysteine molecules onto the Au_{25} cluster. Given the pattern of charge transfers, we speculate that the Coulomb forces holding the atoms together are stronger within the capping staple group than between this and the core Au_{13} cluster. Previous studies combining experiments and simulations also found that the replacement of the SCH_3 groups by SCH_2Cl in the $\text{Au}_{25}(\text{SCH}_3)_{18}$ cluster leads to large charge rearrangements within the capping staple groups, whereas the core Au_c atoms only suffer minor electron transfers [63–67].

Fig. 1h shows the site projected density of states (PDOS) of the $\text{Au}_{25}(\text{SCH}_2\text{CHNH}_2\text{COOH})_{18}$ cluster, illustrating the contribution of each atom. The valence band maximum (VBM), where lies the edge of the highest occupied molecular orbital (HOMO) is dominated by the d states of the core and external Au atoms, which are strongly hybridized between the Fermi level and -7.5 eV. The contribution from the p orbitals of the C, N and O atoms is also noticeable from -1.8 to -10.5 eV with two further narrow bands centred at -11.0 and -13.0 eV. The occupied s orbitals of the H atoms have a similar distribution, although less intense, to the p bands of the C, N and O, in agreement with the covalent bonds formed by them. The PDOS shows shallow bands between the Fermi level and -9.0 eV for the p states of the base and apex S atoms, indicating a strong hybridization and highlighting their

role as linkers of both the Au_{25} cluster and the rest of the cysteine residue. The conduction band minimum (CVM), *i.e.* the boundary of the lowest unoccupied molecular orbital (LUMO), lies at 2.2 eV, with a strong contribution from the p orbitals of the C, N and O atoms and relatively weaker p states of the base S atoms. The contribution from the central Au atom to the density of states is negligible, whereas the virtual bands of the core and external Au, apex S and H atoms is also approximately nil. The calculated HOMO-LUMO gap of 1.3 eV compares well with our experimental value determined using absorption and with previous reports of thiolate protected Au_{25} nanoclusters [62–67]. Also, we have evaluated the partial charge densities within the energy ranges defined by the grey-shaded boxes, which represent the HOMO and LUMO of the nanocluster (Fig. 1i). The DFT calculations suggest that the HOMO is mostly located in the Au and S atoms, whereas, at the same isosurface value, the LUMO only appears around the C, N, O and S atoms, in line with the PDOS.

Tissue penetration of NIR-II fluorescence and renal clearance of Min-23@AuNCs

We assessed the penetration depth limit of NIR-II PL with two types of tissue phantoms: 1) 1% Intralipid® medium; 2) a pork muscle. Firstly, capillary tubes were filled with Min-23@AuNCs or IR-26 and immersed in Intralipid. The capillary profiles display sharp and clear edges at ≤ 3.0 mm beneath the surface of the medium (Fig. 2a). At these depths, the images demonstrate a higher SBR than the threshold *i.e.* $\text{SBR} = 3$ (Fig. 2b). The NIR-II PL of Min-23@AuNCs reaches a penetration depth (δ_1) of 2.90 mm approximately equaling to that (δ_2) of IR-26 *i.e.* $\delta_2 = 2.84$ mm. With the depth increasing, the profiles blurred as a result of light attenuation. The AuNCs has a narrower FWHM (3.56 mm at depth 2.90 mm) than IR-26 (4.09 mm at depth 2.90 mm) to offer higher spatial resolution (Fig. 2b). Secondly, the pork muscle was injected with 50 μL of Min-23@AuNCs and IR-26 at different depths (Fig. 2c). Whilst visually undetectable at 20 mm, the signal from 10 mm deep is still visible. Region-of-interest (ROI) intensity versus depth is fitted according to the Lambert-Beer exponential function (Fig. 2d):

$$T_c = e^{-\mu_t d} \quad (2)$$

where T_c is collimated transmittance; μ_t is total attenuation coefficient; d is tissue thickness. The AuNCs have a 1/e penetration depth (δ'_1) of 6.61 mm – that is, 46% larger than that of IR-26 ($\delta'_2 = 4.64$ mm). Such features are beneficial to the detection of lesions that locate deep in biological tissues. Before moving to *in vivo* studies, Min-23@AuNCs was tested basically nontoxic at the cellular level (Fig. S9a). After intramuscularly injecting 20 μL of the AuNCs into a mouse's rear leg at the depth of 5 mm beneath the skin, the injection site became distinguishable immediately (Fig. 2e). Short-term *in vivo* imaging was conducted upon intravenous (*i.v.*) administration of Min-23@AuNCs (200 μL , 100 $\mu\text{g}/\text{mL}$). Fig. 2f demonstrates the increasing signal of bladder and the faint but unchanged signal of liver. The bladder-to-liver intensity ratio doubles from 2.36 ± 0.02 at 1 min post-injection (*p.i.*) to 4.91 ± 0.04 at 15 min *p.i.*, indicating preferential clearance of the AuNCs through the renal route (Fig. 2g). The bladder achieves about 10-fold higher intensity at 15 min *p.i.* than the liver and background ($P < 0.0001$, Fig. 2h). The plasma

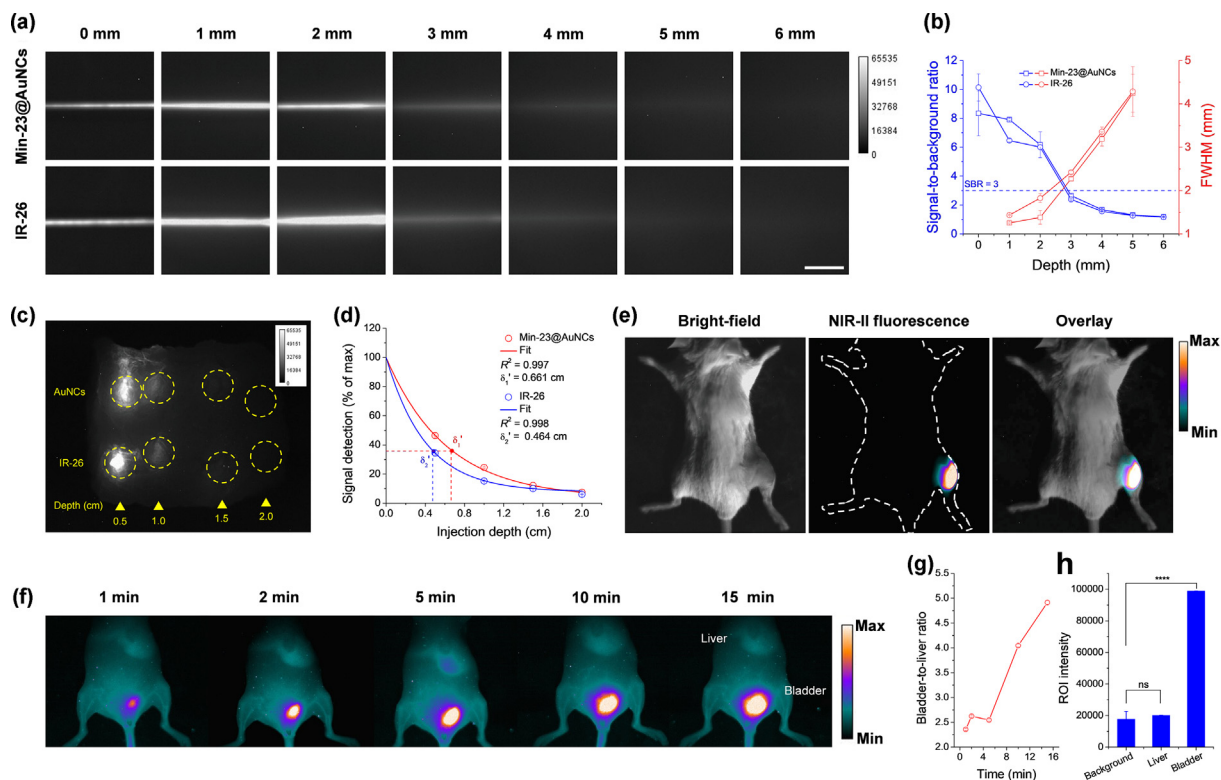


FIGURE 2

Tissue penetration of NIR-II fluorescence and renal clearance of Min-23@AuNCs. (a) Fluorescence images of capillary tubes filled with Min-23@AuNCs or IR-26, immersed in 1% Intralipid[®] solution at the depth of 0, 1, 2, 3, 4, 5, and 6 mm. The fluorescence signals are collected in the NIR-II (1000–1700 nm) region upon 808-nm laser excitation with a 1000-nm long-pass filter. Scale bar, 10 mm. (b) Signal-to-background ratio (SBR) and full-width-half-maximum (FWHM) of capillary tube intensity plotted as a function of depth. The threshold for distinguishing signal from background noise is set at SBR = 3 (blue dash line). (c) Fluorescence image of a pork muscle tissue injected with 50 μ L of Min-23@AuNCs and 50 μ L of IR-26 (control) at different depths *i.e.* 0.5, 1, 1.5, and 2 cm. (d) Percentage of measured region-of-interest (ROI, marked by a dashed circle) signal to the extrapolated one of tissue surface plotted as a function of injection depth. The data are perfectly fitted to a monoexponential decay ($R^2 > 0.99$), giving the $1/e$ penetration depth $\delta'_1 = 0.661$ cm for Min-23@AuNCs and $\delta'_2 = 0.464$ cm for IR-26. (e) Bright-field, dark-field and overlay images of a BALB/c wide-type mouse submuscularly injected with 50 μ L of Min-23@AuNCs into the muscle of right rear leg. (f) Time-lapse fluorescence images of a mouse in its supine position intravenously injected with 200 μ L of Min-23@AuNCs (100 ms exposure time, 15 min imaging period). (g) Bladder-to-liver intensity ratio plotted as a function of time at post-injection (*p.i.*). (h) ROI intensity of background, liver and bladder at 15 min *p.i.* The data are expressed as the mean \pm standard deviation (s.d.) for $n = 3$ per condition and compared using Student t-test. Significant differences are indicated by asterisks: ****= $P < 0.0001$, and ns = non-significance ($P > 0.05$).

concentration-versus-time profile determined by inductively coupled plasma mass spectrometry (ICP-MS) is fitted by a two-compartment model ($R^2 = 0.98$) with a moderately long distribution half-life ($t_{1/2\alpha}$) of 14.9 min and a short elimination half-life ($t_{1/2\beta}$) of 3.1 h (Fig. S10).

Preparation of NR@Min-23@AuNCs for smartphone-triggered PDT at the cellular level

Unlike the AuNCs reported by Kawasaki et al., [26] Min-23@AuNCs can hardly produce $^1\text{O}_2$ under visible light ($\lambda = 532$ nm) irradiation (Fig. S11), where the $^1\text{O}_2$ level was determined by the absorption decay of 9,10-anthracenediyl-bis(methyl-ene)dimalonic acid (ABDA). For this reason, we engineered an azido derivative of NR for the functionalization of Min-23@AuNCs (Fig. S12) [68]. NR on the AuNC surface acts as antenna to strengthen the $^1\text{O}_2$ generation, while the AuNCs improve the solubility of NR in aqueous media with improved pharmacokinetics. Fig. 3a depicts the two-step click conjugation process. First, DBCO-PEG-modified Min-23@AuNCs (abbrevia-

tion as DBCO-PEG4@Min-23@AuNCs) were formed by reacting DBCO-PEG4-NHS ester with Min-23@AuNCs, where the active NHS ester reacted specifically with primary amines in the lysine (K) residue and on the N-terminus (not shown in the scheme) of Min-23 ligand to form a covalent amide linkage and released NHS as a leaving group. Secondly, NR was added into DBCO-PEG4@Min-23@AuNCs and incubated at room temperature, during which NR was efficiently conjugated onto DBCO-PEG4@Min-23@AuNCs covalently *via* the Cu-free click reaction between azide and DBCO to form NR@Min-23@AuNCs. The question then arises as to how much NR ought to be loaded. On the one hand, the maximal load requires grafting as many PEGylated linkers as possible on the AuNC surface with increasing size (abbreviated as “full-load” NR@Min-23@AuNCs); on the other hand, the partial load such as $\sim 50\%$ less NR than the “full-load” (abbreviated as NR@Min-23@AuNCs) compromises the therapeutic effect, but this issue can be addressed by increasing the dosage per treatment. We summarize in Table S2 the primary parameters of Min-23@AuNCs, NR@Min-23@AuNCs and “full-

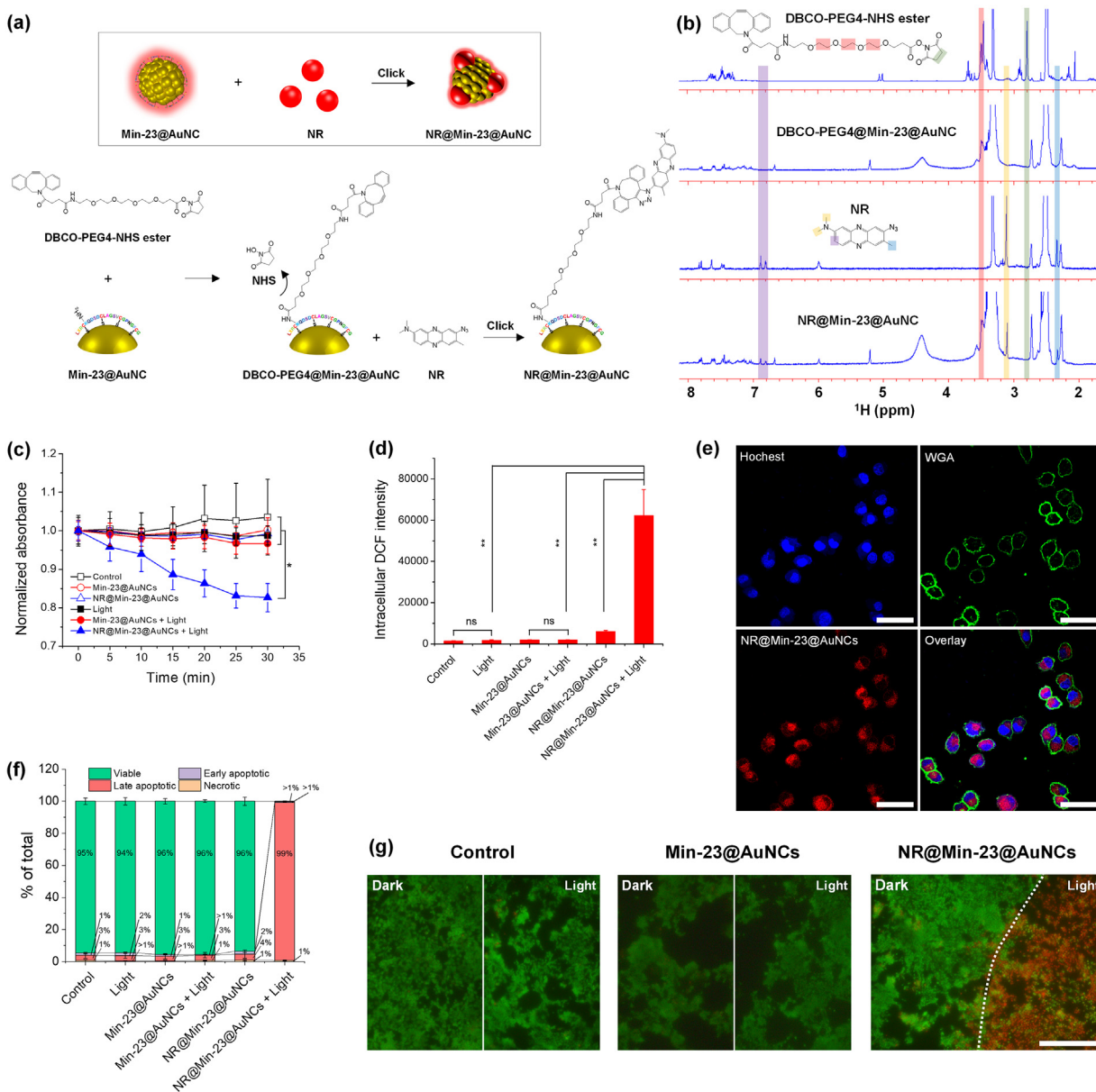


FIGURE 3

Preparation of NR@Min-23@AuNCs for smartphone-triggered PDT at the cellular level. (a) Schematic illustration of "clicking" NR onto Min-23@AuNCs with DBCO-PEG4-NHS ester via the intermediate DBCO-PEG4@Min-23@AuNCs. Boxed panel: the simplified scheme. (b) ^1H NMR spectra of DBCO-PEG4-NHS ester, DBCO-PEG4@Min-23@AuNC, NR and NR@Min-23@AuNC in DMSO- d_6 (the strong peak at 2.5 ppm in the spectra). Note that H_2O residue peak appears at 3.3 ppm as a single peak in the spectra. (c) Time-lapse absorbance at 380 nm of ABDA incubated with Min-23@AuNCs or NR@Min-23@AuNCs in D_2O placed in darkness or under the irradiation, where "the irradiation" represents 30-min smartphone's torch irradiation (fluence rate: $8 \text{ mW}/\text{cm}^2$; radiant exposure: $14.4 \text{ J}/\text{cm}^2$). (d) Quantification of ROS level within 4T1 cells with or without the irradiation. The cells were pre-incubated with DMEM (control), Min-23@AuNCs or NR@Min-23@AuNCs for 2 h, and then stained with the ROS probe DCFDA. The signals were collected by a microplate reader. (e) Confocal laser scanning microscopy (CLSM) analysis of 4T1 cells co-stained with Hoechst (nucleus tracker), wheat germ agglutinin (WGA)-Alexa Fluor 488 conjugate (plasma membrane tracker) and NR@Min-23@AuNCs. The cells were incubated at 37°C with the dyes for 30 min in the serum-free medium and then washed with PBS before imaging. Scale bar, $40 \mu\text{m}$. (f) Percentage of viable, apoptotic and necrotic cells subjected to the indicated treatments, measured by flow cytometry. The data are expressed as the mean \pm s.d. for $n = 3$ per condition and compared using one-way ANOVA test. Significant differences are indicated by asterisks: $*P < 0.05$, $**P < 0.01$, and ns = non-significance ($P > 0.05$). (g) Microscopic detection of apoptosis using AO/PI double staining. Note that the dashed line outlines the boundary between non-irradiated and neighboring irradiated area on exposure to $100 \mu\text{g}/\text{mL}$ NR@Min-23@AuNCs. Scale bar, $500 \mu\text{m}$.

load" NR@Min-23@AuNCs. Considering a strategic balance, NR@Min-23@AuNCs were chosen as the focus of the present study. The quantitation of available binding sites is a prerequisite for accurate control of the covalent crosslinking. The concentration of reactive amine groups in the Min-23 ligands were accordingly estimated to be $0.035 \mu\text{mol}$ per $10 \mu\text{L}$ of the Min-23@AuNC

solution by colorimetric ninhydrin reaction (Fig. S13). The NR density (σ) on the AuNC surface is calculated to be $0.24/\text{nm}^2$ by equation (3),

$$\sigma = \frac{[\text{NR}]_{\text{conj}}}{4\pi R^2 [\text{AuNC}]} \quad (3)$$

where R is the core radius ($R = 0.91$ nm) of AuNC; $[AuNC]$ is the molar concentration ($[AuNC] \approx 0.19$ mM) of Min-23@AuNCs; $[NR]_{conj}$ is the molar concentration ($[NR]_{conj} \approx 0.48$ mM) of the conjugated NR (*i.e.* equivalent to ~ 2.5 copies of NR on each AuNC). To provide evidence of successful crosslinking, we performed proton nuclear magnetic resonance (1H NMR) spectroscopic analysis on NR@Min-23@AuNCs and its intermediate – DBCO-PEG4@Min-23@AuNCs. The characteristic succinimidyl peak of NHS at 2.8 ppm in the pure crosslinker disappeared completely in DBCO-PEG4@Min-23@AuNCs (Fig. 3b), while the methylene peak of the PEG chain at 3.50 ppm were found in both samples. The result indicates the covalent linkage of DBCO-PEG4-onto Min-23@AuNCs. Moreover, comparing the NMR spectra of DBCO-PEG4@Min-23@AuNCs and NR@Min-23@AuNCs, it is clear that the characteristic peaks of NR at 2.3, 3.1, 6.8 and 6.9 ppm appeared in the latter. Together, the NMR results provide the definitive evidence for successful covalent conjugation of NR onto Min-23@AuNCs as proposed *via* the DBCO-PEG4-NHS ester crosslinker. Despite the covalent grafting of PEG chains, the hydrodynamic diameter (D_h) of NR@Min-23@AuNCs is ~ 6.4 nm which is still comparable to the KFT (Table S2). Their surface charge can also promote renal clearance, benefitting from positively charged NR (Fig. S14).

The *in vitro* 1O_2 productivity of NR@Min-23@AuNCs was gauged under smartphone's torch irradiation (fluence rate: 8 mW/cm 2). There is a large overlap between the torch emission and the NR absorption spectra (Fig. S15). After 30 min irradiation (radiant exposure: 14.4 J/cm 2 , hereafter referred to as the irradiation), $\sim 20\%$ of ABDA (initial concentration: 50 μ M) were oxidized (Fig. 3c). The detectable 1O_2 accounts for merely $\sim 2\%$ of the total [69], so the adjusted 1O_2 production rate reaches 1.0 mM/h. Without either NR or the irradiation, ABDA stayed unoxidized. As NR is a type-I PS, NR@Min-23@AuNCs allow for production of various ROS (*e.g.*, $O_2^{\cdot-}$, $\cdot OH$, H_2O_2 , *etc.*) other than 1O_2 . The intracellular ROS was quantified using the fluorescence “turn-on” ROS probe 2',7'-dichlorodihydrofluorescein diacetate (DCFDA). The cells subjected to the combined, but not individual, use of the irradiation and NR@Min-23@AuNCs show over 10-fold level of ROS compared with the cells subjected to either alone (Fig. 3d).

To the best of our knowledge, a commercial high-resolution NIR-II microscope has not yet been available. We therefore visualized NR@Min-23@AuNCs inside cells with conventional laser scanning confocal microscopy by detecting the bounded NR ($\lambda_{em} = 614$ nm). The plasma membranes were stained green by wheat germ agglutinin conjugated Alexa Fluor 488, while the nuclei were stained blue by Hoechst. The red-emitting NR throughout the cytoplasm helped locate the intracellular NR@Min-23@AuNCs (Fig. 3e). The cells remained $>90\%$ of viability upon exposure to NR@Min-23@AuNCs (200 μ g/mL) due to low dark toxicity (Fig. S9b). Once torch light was shined on, $99.6 \pm 0.2\%$ of the cells died immediately (Fig. 3f and Fig. S16a) even though NR@Min-23@AuNCs were diluted to 100 μ g/mL (equivalent to ~ 15 μ g/mL NR). Likewise, NR alone (15 μ g/mL) killed $\sim 99\%$ of cells under the irradiation (Fig. S16b). Consistent with the ROS measurement, Min-23@AuNCs posed neither dark- nor photo-toxicity with $\approx 96\%$ of viable cells. Viability assay using acridine orange (AO) and pro-

pidium iodide (PI) shows a distinct boundary between non-irradiated and neighboring irradiated cells incubated with NR@Min-23@AuNCs (Fig. 3g). The smartphone's torch was as powerful as a high-level LED lamp (fluence rate: 96 mW/cm 2 , radiant exposure: 172.8 J/cm 2) that both can saturate the photo-toxicity (Figs. S16c–S16e).

NIR-II *in vivo* imaging with NR@Min-23@AuNCs

With *i.v.* injection of Min-23@AuNCs, NR@Min-23@AuNCs or “full-load” NR@Min-23@AuNCs, time-course NIR-II *in vivo* imaging was carried out to track their biodistribution in mice bearing subcutaneous 4T1 tumors. The autofluorescence background is minimized to a barely detectable level at pre-injection whereas the whole bodies become intensely fluorescent at 0.5 h *p.i.* (Fig. 4a). Min-23@AuNCs flew into urine with the strongest signal from the bladder, similar to their behavior in the healthy mice. *Ex vivo* whole-organ imaging (Fig. 4a) and the quantitative analysis of fluorescence in tissues (Fig. 4b) validate the primary clearance of Min-23@AuNCs by the kidneys with no tumor uptake. In contrast, NR@Min-23@AuNCs accumulated in tumors with excellent specificity *via* the EPR effect (Fig. 4a) so that the tumors became truly distinguishable from other tissues (Fig. S17). Compared with “full-load” NR@Min-23@AuNCs, however, a large amount of NR@Min-23@AuNCs were spared from the liver and the spleen to end up in the kidneys for efficient renal clearance. The increasing D_h of “full-load” NR@Min-23@AuNCs in plasma gave rise to the severe RES sequestration (Fig. S18). Regarding the difference in the *in vivo* biodistribution of Min-23@AuNCs ($D_h = 3.7$ nm) and NR@Min-23@AuNCs ($D_h = 6.4$ nm), the former is fairly below the KFT, so it underwent rapid renal elimination; whereas the latter is right on the KFT, which allowed for prolonged blood circulation and tumor passive targeting *via* the EPR effect yet still renal clearable. The weak signals from brain tissues indicate that there was only a minimum amount of NR@Min-23@AuNCs crossing the BBB. Tumor-to-background ratio (TBR) remained above the Rose criterion (TBR = 5) for at least 6 h and escalated in a ~ 6 -fold increment to 7.0 ± 0.3 at 4 h *p.i.* for easily locating the tumor (Fig. 4c). With the PEGylated linkers grafting on the AuNC surface, NR@Min-23@AuNCs have a prolonged $t_{1/2\beta} = 6.3 \pm 0.8$ h (Fig. 4d), which warrants the sufficient transport to the tumors. Despite being both renally and hepatically clearable, NR@Min-23@AuNCs in urine exceeds 56.1% injected dose (ID) at 12 h *p.i.* (Fig. 4e), ~ 38 fold more than that in feces *i.e.* 1.5% ID. Their cumulative amount approximates to 80% ID at 48 h *p.i.* versus merely 15% ID of plasmonic AuNPs (size ≈ 16 nm) [70]. We presume accordingly that, if rapid renal clearance is overemphasized with a small size (*e.g.*, Min-23@AuNCs), it will emasculate tumor targeting efficiency due to weak EPR effect [71]; if effective tumor targeting is pursued with a large size (*e.g.*, “full-load” NR@Min-23@AuNCs), it will lead to severe RES deposition. In this regard, NR@Min-23@AuNCs appear to be an optimal choice.

Smartphone-triggered *in vivo* PDT against tumors with NR@Min-23@AuNCs

Before *in vivo* PDT experiments, we have performed additional blood testing and histologic examinations in mouse models to investigate the potential *in vivo* systemic toxicity of NR@Min-

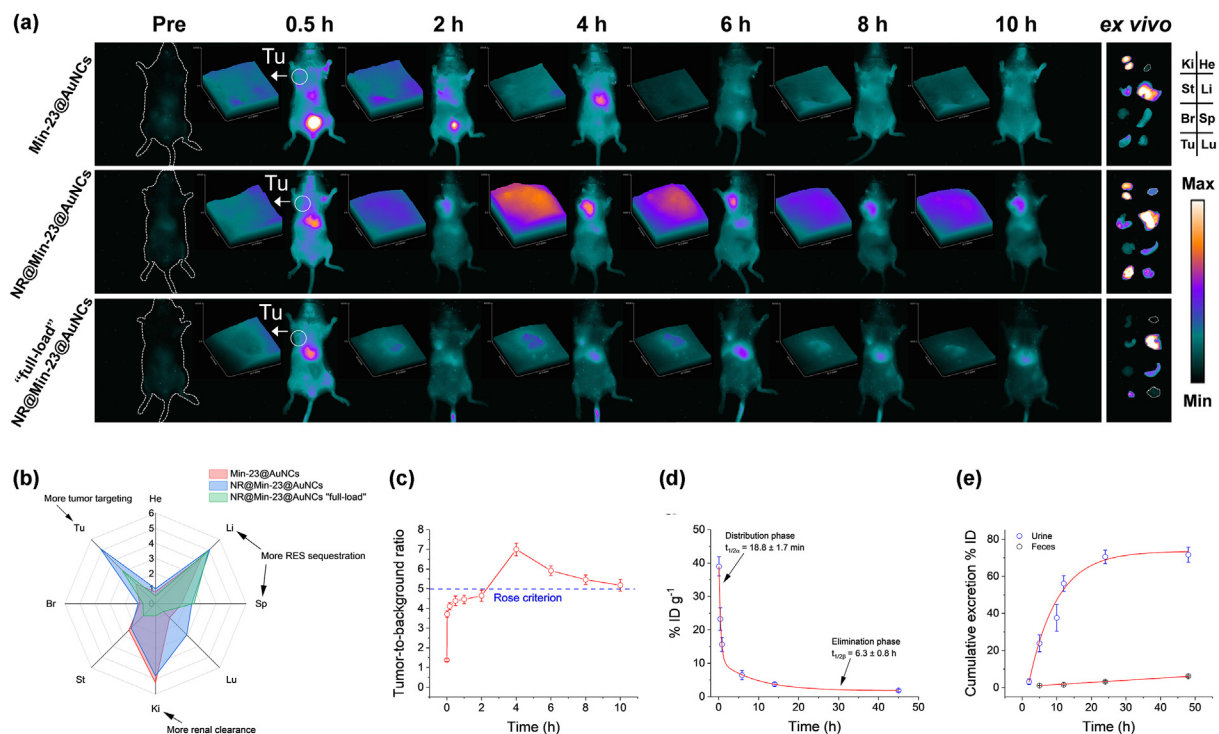


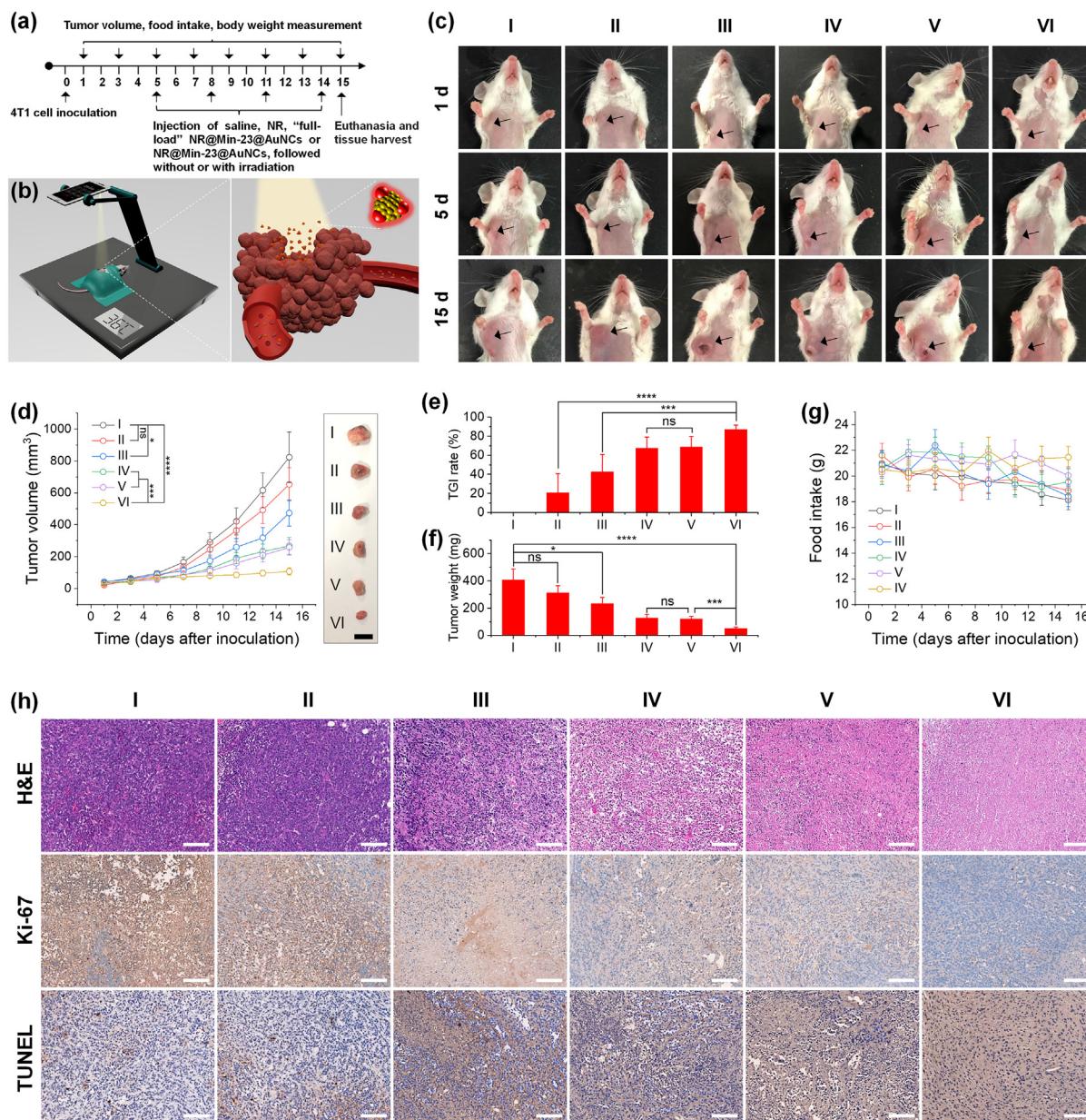
FIGURE 4

NIR-II *in vivo* imaging and body clearance. (a) Time-lapse *in vivo* and *ex vivo* NIR-II imaging of 4T1 tumor-bearing mice intravenously injected with 200 μL of Min-23@AuNCs, NR@Min-23@AuNCs or "full-load" NR@Min-23@AuNCs under excitation at 808 nm (150 mW/cm², 100 ms exposure) with a 1000 nm long-pass (LP) filter, showing preferential tumor accumulation of NR@Min-23@AuNCs with an enhanced contrast. Insets are the 3D surface plot images to demonstrate the fluorescence intensity of tumors. Abbreviation: He, heart; Li, liver; Sp, spleen; Lu, lung; Ki, kidney; St, stomach; Br, brain; Tu, tumor. (b) Corresponding fluorescence intensity ratio of harvested major organs to background (muscle). Abbreviation: He, heart; Li, liver; Sp, spleen; Lu, lung; Ki, kidney; St, stomach; Br, brain; Tu, tumor. (c) Plot of tumor-to-background intensity ratio (TBR) as a function of time *p.i.* for the NIR-II images of mouse injected with NR@Min-23@AuNCs, where the tumor becomes distinguishable from 2 to 10 h *p.i.*, according to the TBR above the Rose criterion (TBR = 5). (d) Plasma pharmacokinetic profile of NR@Min-23@AuNCs in mice over a time span of 0–45 h after *i.v.* injection, which is perfectly fitted ($R^2 = 0.99$) to a bi-exponential decay function, giving a distribution half-life $t_{1/2\alpha}$ of 18.8 ± 1.7 min and an elimination half-life $t_{1/2\beta}$ of 6.3 ± 0.8 h. (e) Cumulative renal and hepatic excretions of NR@Min-23@AuNCs during a post-injection period of 48 h, measured by ICP-MS. The data are expressed as the mean \pm s.d. for $n = 3$ per condition.

23@AuNCs (Figs. S19–S21). There are conclusive reasons to believe that NR@Min-23@AuNCs are highly biocompatible (see detailed discussion in Supplementary Material). Moreover, the rise in the temperature of the solution containing NR@Min-23@AuNCs was not evident and there was no significant variation in the skin temperature of mice received *i.v.* injection of NR@Min-23@AuNC under the smartphone's torch irradiation (Fig. S22), confirming that the nanocluster can hardly convert the torch light (wavelength: 400–750 nm) into heat.

Monitoring of tumor volume as a function of time reveals tumor suppression by NR, "full-load" NR@Min-23@AuNCs or NR@Min-23@AuNCs with a regimen of smartphone's LED torch irradiation delivered at a prescribed light dose of 28.8 J/cm² (hereafter also referred to as 2 \times irradiation), where we extended the duration of irradiation to compensate light attenuation and scattering by the skin. Fig. 5a illustrates the general procedures: (1) mice are inoculated with 4T1 cells on day 0; (2) after palpable tumors growing to ~ 70 mm³ on day 5, the mice are divided into six groups ($n = 5$, in each group) and treated, respectively, with (I) saline as the control, (II) NR@Min-23@AuNCs alone, (III) NR alone, (IV) NR + 2 \times irradiation, (V) "full-load" NR@Min-23@AuNCs + 2 \times irradiation, and (VI) NR@Min-23@AuNCs + 2 \times irradiation;

(3) tumor size, food intake and body weight are measured every 2 days before euthanasia on day 15 for tissue sampling. Note that: (1) *i.v.* administration is applied to all the injectants expect for NR that needs to be injected intratumorally because of poor aqueous solubility; (2) Min-23@AuNCs have been verified at the cellular level without either dark- or photo-toxicity, so it is unnecessary to be evaluated on animal models. The torch light was shone on the tumor area with the rest body parts covering by a non-transparent film so as to minimize off-target toxicity (Fig. 5b). The digital photographs recorded the gross appearance of 4T1 primary tumors in response to different treatments. Starting as a tiny and pimple-like lesion, most tumors developed into a dome-shaped nodule during the first 5 days after inoculation (Fig. 5c). Since then, until the scheduled euthanasia, the tumor burden was monitored by volume calculation using caliper measurement (Fig. 5d). The tumor volume doubling times in Groups I and II were 3.4 and 3.8 days, respectively; and their volumes at 10 days after the first treatment were statistically indistinguishable (average volume: 823 ± 158 mm³ versus 653 ± 105 mm³, $P > 0.05$). On the contrary, the tumors directly injected with NR grew slowly with the volume (473 ± 82 mm³, Group III; 267 ± 54 mm³, Group IV) dramatically smaller than

**FIGURE 5**

Smartphone-triggered *in vivo* PDT on tumors. (a) Flowchart and timeline illustrating the schedule and procedures. (b) Schematic illustrations of (left) an experimental setup for the PDT on a 4T1 tumor-bearing mouse and (right) a collapsed tumor tissue resulting from the PDT. (c) Photographs of tumor-bearing mice on day 1, day 5, and day 15 of a 15-day course. The mice are divided into six groups and treated, respectively, with (i) saline, (ii) NR@Min-23@AuNCs, (iii) NR, (iv) NR + 2 \times irradiation, (v) “full-load” NR@Min-23@AuNCs + 2 \times irradiation, and (vi) NR@Min-23@AuNCs + 2 \times irradiation. “2 \times irradiation” represents 60-min smartphone’s LED torch irradiation (fluence rate: 8 mW/cm²; radiant exposure: 28.8 J/cm²). Black arrows locate tumors. (d) Tumor growth curves of mice in Groups I–VI subjected to the indicated treatment (left panel) and the photograph of resected tumors at the end of the experiment (right panel). (e) Percent tumor growth inhibition (% TGI) and (f) tumor weight of mice at time of sacrifice. The data are expressed as the mean \pm s.d. for $n = 5$ per treatment group and compared using one-way ANOVA test. Significant difference is indicated by asterisks: * $P < 0.05$, ** $P < 0.01$, **** $P < 0.0001$ and ns = non-significance ($P > 0.05$). (g) Food intake per group as a function of time throughout the treatments. (h) H&E, Ki-67 staining and TUNEL assay of tumor tissues harvested at time of sacrifice. Scale bar, 100 μ m.

that in the control group ($P < 0.05$), even in the absence of 2 \times irradiation. When given repeatedly, the high dark toxicities of NR and DMSO that used for dissolving NR were responsible for the anti-tumor activity observed in Group III [72]. The tumors became black-colored with a crater-like appearance because of necrotizing dermatitis (Fig. 5c). Without being diluted by the

blood pool, the NR concentration in the tumors in Group IV was higher than Groups V and VI. However, NR alone inhibited tumor growth to a similar level to that of “full-load” NR@Min-23@AuNCs (volume: 257 ± 48 mm³) but lower than NR@Min-23@AuNCs (volume: 107 ± 21 mm³). The difference arises from the aggregation of NR in bio-fluids. Additionally, prolonging

the irradiation from 0.5 h to 1 h can suppress the tumors to a greater extent (Fig. S23a). In clinical practice, long-time irradiation might be inconvenient for physicians to manage with and probably cause discomfort to patients, such as muscle stiffness due to limited range of motion for an extended period of time. We have come up with two solutions to this issue: (1) A wearable phone mount can be used for placing the smartphone directly on the tumor for continuous irradiation, during which patients can freely move their body segment; however, it seems not every part of the body where a lesion occurs is ideally suited to the phone mount, such as armpit; (2) Increasing the frequency and duration of the PDT treatment could be another effective way to maintain a favorable therapeutic outcome while reducing the irradiation time; this, though, might mean more hospital visits and higher medical cost for patients. Obviously, each solution has its own pros and cons, and to decide which one is better will depend on patients' situation and needs. Benefiting from the high efficiency and homogeneity of tumor targeting, the light-activated NR@Min-23@AuNCs yielded the highest tumor growth inhibition (TGI) rate ($\approx 90\%$), and moreover the maximal significant difference was observed between Groups I and VI (Fig. 5e, $P < 0.0001$). The weight of resected tumors consistently reflects the volume measurement, where the mice in Group VI have more than 87% reduction in the tumor weight (Fig. 5f). The tumor burden depressed food intake in Groups I–V by 5–10% (Fig. 5g), while the Group VI mice appeared to be healthier without weight loss (Fig. S23b).

Hematoxylin and eosin (H&E), Ki-67 immunohistochemistry staining and TUNEL assay of tumor tissues are further evidence for the highest rate of cell death in Group VI (Fig. 5h). The histological analysis shows nuclei are either vacuolated or shrunken in the experimental groups, especially Group VI in which few nuclei were found morphologically intact. Sharp decrease in the Ki-67 level occurred to the tissue subjected to the combined use of NR@Min-23@AuNCs and $2 \times$ irradiation, indicating that the proliferative activity was markedly inhibited. The ratio of TUNEL-positive apoptotic cells in Group VI is largest among all experimental groups. Conclusively, NR@Min-23@AuNCs has the most powerful antitumor effects. Unnoticeable abnormality in the H&E staining of organs harvested at the time of sacrifice indicates that all the treatments induced undetectable levels of systemic toxicity (Fig. S24).

Conclusion

In summary, we have demonstrated a rapid, efficient and microwave-assisted approach for preparing AuNCs capped with zwitterionic Min-23. Min-23@AuNCs fluoresce strongly in the NIR-II region with a D_h nearly 30% below the KFT for rapid renal clearance. Using the $\text{Au}_{25}(\text{SCH}_2\text{CHNH}_2\text{COOH})_{18}$ cluster model, the physico-chemical properties were investigated computationally. The thermodynamics of formation was modelled and we found that to be an exothermic process. The analysis of the charge transfers suggests that the Au and S atoms forming the staple groups play a prominent role in the electron charge density pathway. The calculated projected density of states indicates that the HOMO is located at the core Au and base S atoms, whereas the LUMO appears mostly in the cysteine fragments.

The primary amine groups on Min-23@AuNCs was quantified by the ninhydrin assay in order to control the covalent binding with NR *via* “click” reaction. Without the need for a targeting moiety, NR@Min-23@AuNCs preferentially accumulate in tumors by exploiting the EPR effect and also induce a $\sim 90\%$ reduction of tumor size under smartphone's torch irradiation. We believe that the methodologies presented in this work would represent a critical step in designing effective theranostic nanomedicines with great potential for clinical translation.

Material and methods

For experimental details, see [Supplementary Material](#).

Data availability

The data that supports the findings of this study are available in the [supplementary material](#) of this article.

Acknowledgements

We acknowledge the Engineering and Physical Sciences Research Council (EPSRC grant number EP/K009567) for funding. *Via* our membership of the UK's HEC Materials Chemistry Consortium, which is funded by EPSRC (EPSRC grant numbers EP/L000202, EP/R029431, EP/T022213), this work used the ARCHER UK National Supercomputing Service (<http://www.archer.ac.uk>). This work was undertaken on ARC4, part of the High-Performance Computing facilities at the University of Leeds, United Kingdom. This work also used the Supercomputing Facilities at Cardiff University operated by the Advanced Research Computing @ Cardiff (ARCCA) Division on behalf of the Supercomputing Wales (SCW) project, which is part-funded by the European Regional Development Fund (ERDF) *via* the Welsh Government. This work was also supported by (1) Department of Defense/Air Force Office of Scientific Research Military Photomedicine Program (FA9550-17-1-0277), American Cancer Society (132998-MBG-18-208-01) and Department discretionary funds to M.X.W; (2) the UK Biotechnology and Biological Sciences Research Council (BBSRC, grant no: BB/R007829/1) to D.Z. We also acknowledge the help of Dr Dehua Huang, Dr Yejun Zhang and Prof. Qiangbin Wang from Suzhou Institute of Nano-tech and Nano-bionics, Chinese Academy of Sciences with *in vivo* imaging.

CRediT authorship contribution statement

Yifei Kong: Conceptualization, Methodology, Validation, Investigation, Data curation, Writing – original draft, Writing – review & editing, Project administration. **David Santos-Carballal:** Software, Formal analysis, Writing – original draft, Resources, Funding acquisition. **David Martin:** Investigation, Validation. **Natalia N. Sergeeva:** Investigation, Validation. **Weili Wang:** Validation, Investigation, Project administration. **Guishi Liu:** Investigation. **Benjamin Johnson:** Investigation, Validation. **Brijesh Bhayana:** Validation. **Zuantao Lin:** Investigation. **Yensheng Wang:** Investigation. **Xavier Le Guével:** Writing – review & editing, Supervision. **Nora H. de Leeuw:** Writing – review & editing, Resources, Funding acquisition. **Dejian Zhou:** Writing – review & editing, Supervi-

sion, Funding acquisition. **Mei X. Wu:** Writing – review & editing, Supervision, Resources, Funding acquisition.

Declaration of Competing Interest

The authors declare that they have no known competing financial interests or personal relationships that could have appeared to influence the work reported in this paper.

Appendix A. Supplementary data

Supplementary data to this article can be found online at <https://doi.org/10.1016/j.mattod.2021.09.022>.

References

- [1] O.C. Farokhzad, R. Langer, *ACS Nano* 3 (1) (2009) 16.
- [2] V. Chauhan et al., *Nat. Nanotechnol.* 7 (6) (2012) 383.
- [3] E.-K. Lim et al., *Chem. Rev.* 115 (1) (2015) 327.
- [4] G. Chen et al., *Chem. Rev.* 116 (5) (2016) 2826.
- [5] C. Liang et al., *Chem. Soc. Rev.* 45 (22) (2016) 6250.
- [6] M.S. Muthu et al., *Theranostics* 4 (6) (2014) 660.
- [7] X. Qu et al., *Nano Res.* 12 (3) (2019) 593.
- [8] S. Kunjachan et al., *Chem. Rev.* 115 (19) (2015) 10907.
- [9] US Food and Drug Administration, *Part 1: Conducting Safety Assessments, Final Guidance: Developing Medical Imaging Drug and Biological Products* (2004), pp.5, URL: <https://www.fda.gov/drugs/development-resources/medical-imaging-and-drug-development..>
- [10] D.A. Giljohann et al., *Angew. Chem. Int. Ed.* 19 (49) (2010) 3280.
- [11] A. Thakor et al., *Nano Lett.* 11 (10) (2011) 4029.
- [12] C.M. Cobley et al., *Chem. Soc. Rev.* 40 (1) (2011) 44.
- [13] H. Liu et al., *Adv. Mater.* 31 (46) (2019) 1901015.
- [14] L. Song et al., *Adv. Healthcare Mater.* 2 (2) (2013) 380.
- [15] S.K. Libutti et al., *Clin. Cancer Res.* 16 (24) (2010) 6139.
- [16] K.L. Aillon et al., *Adv. Drug Deliv. Rev.* 61 (6) (2009) 457.
- [17] H.S. Choi et al., *Nat. Biotechnol.* 25 (10) (2007) 1165.
- [18] J. Liu et al., *Angew. Chem. Int. Ed.* 125 (48) (2013) 12804.
- [19] M. Yu, J. Zheng, *ACS Nano* 9 (7) (2015) 6655.
- [20] B. Du et al., *Nat. Nanotechnol.* 12 (11) (2017) 1096.
- [21] B. Du et al., *Nat. Rev. Mater.* 3 (10) (2018) 358.
- [22] C. Zhang et al., *Adv. Funct. Mater.* 25 (8) (2015) 1314.
- [23] J. Meng et al., *J. Neuroimmune Pharmacol.* 12 (1) (2017) 84.
- [24] C. Zhou et al., *Angew. Chem. Int. Ed.* 50 (14) (2011) 3168.
- [25] J. Liu et al., *J. Am. Chem. Soc.* 135 (13) (2013) 4978.
- [26] H. Kawasaki et al., *Chem. Mater.* 26 (9) (2014) 2777.
- [27] Q. Chen et al., *Nano Res.* 11 (10) (2018) 5657.
- [28] X.-D. Zhang et al., *Biomaterials* 33 (18) (2012) 4628.
- [29] Z. Hu et al., *Nat. Biomed. Eng.* 4 (3) (2020) 259.
- [30] A.M. Smith et al., *Nat. Nanotechnol.* 4 (11) (2009) 710.
- [31] S. Diao et al., *Nano Res.* 8 (9) (2015) 3027.
- [32] G. Hong et al., *Nat. Biomed. Eng.* 1 (1) (2017) 1.
- [33] F. Wang et al., *Nat. Methods* 16 (6) (2019) 545.
- [34] C. Li, Q. Wang, *ACS Nano* 12 (10) (2018) 9654.
- [35] W. Poon et al., *ACS Nano* 13 (5) (2019) 5785.
- [36] G. Hong et al., *Nat. Photonics* 8 (9) (2014) 723.
- [37] G. Hong et al., *Nat. Med.* 18 (12) (2012) 1841.
- [38] A.L. Antaris et al., *Nat. Mater.* 15 (2) (2016) 235.
- [39] J.A. Carr et al., *Proc. Natl. Acad. Sci.* 115 (17) (2018) 4465.
- [40] D. Cui et al., *Adv. Mater.* 32 (6) (2020) 1906314.
- [41] Y. Fan et al., *Nat. Nanotechnol.* 13 (10) (2018) 941.
- [42] Y. Kong et al., *Chem. Mater.* 28 (9) (2016) 3041.
- [43] Y. Zhang et al., *ACS Nano* 6 (5) (2012) 3695.
- [44] X. Le Guevel et al., *Nanoscale* 6 (14) (2014) 8091.
- [45] B. Musnier et al., *Nanoscale* 11 (25) (2019) 12092.
- [46] Z. Yu et al., *ACS Nano* 14 (4) (2020) 4973.
- [47] Y. Chen et al., *Nano Lett.* 17 (10) (2017) 6330.
- [48] E.G. Baker et al., *Acc. Chem. Res.* 50 (9) (2017) 2085.
- [49] C. Souriau et al., *Biochemistry* 44 (19) (2005) 7143.
- [50] F. Zoller et al., *ChemMedChem* 7 (2) (2012) 237.
- [51] F. Aldeek et al., *ACS Nano* 7 (3) (2013) 2509.
- [52] D. Mishra et al., *PCCP* 21 (38) (2019) 21317.
- [53] B.B. Fischer et al., *Environ. Sci. Technol.* 38 (23) (2004) 6307.
- [54] O'Dea S, *Numbers of Smartphone Users Worldwide from 2016 to 2021* (2020) URL: [https://www.statista.com/statistics/330695/number-of-smartphone-users-worldwide/..](https://www.statista.com/statistics/330695/number-of-smartphone-users-worldwide/)
- [55] J. Hempstead et al., *Sci. Rep.* 5 (1) (2015) 1.
- [56] K. Welsher et al., *Proc. Natl. Acad. Sci.* 108 (22) (2011) 8943.
- [57] Y. Zhong et al., *Nat. Biotechnol.* 37 (11) (2019) 1322.
- [58] J.L. Fajin et al., *Langmuir* 29 (28) (2013) 8856.
- [59] G. Rajaraman et al., *J. Mater. Chem.* 20 (47) (2010) 10747.
- [60] G. Yao, Q. Huang, *J. Phys. Chem C* 122 (27) (2018) 15241.
- [61] M.W. Heaven et al., *J. Am. Chem. Soc.* 130 (12) (2008) 3754.
- [62] M. Zhu et al., *J. Am. Chem. Soc.* 130 (18) (2008) 5883.
- [63] J.F. Parker et al., *J. Phys. Chem. C* 114 (18) (2010) 8276.
- [64] J. Jung et al., *Nanoscale* 4 (14) (2012) 4206.
- [65] D.R. Kauffman et al., *Chem. Sci.* 5 (8) (2014) 3151.
- [66] J. Akola et al., *J. Am. Chem. Soc.* 130 (12) (2008) 3756.
- [67] J. Schacht, N. Gaston, *ChemPhysChem* 17 (20) (2016) 3237.
- [68] D. Billy, *Chem. Commun.* 53 (77) (2017) 10715.
- [69] T. Entradas et al., *J. Photochem. Photobiol., B* 204 (2020) 111787.
- [70] L.Y. Chou et al., *Nat. Nanotechnol.* 9 (2) (2014) 148.
- [71] X. Song et al., *Angew. Chem. Int. Ed.* 60 (3) (2021) 1306.
- [72] J. Galvao et al., *FASEB J.* 28 (3) (2014) 1317.